Experimental demonstration of >20 kJ laser energy coupling in 1-cm hydrocarbon-filled gas pipe targets via inverse Bremsstrahlung absorption with applications to MagLIF

B. B. Pollock, C. Goyon, A. B. Sefkow, et al.
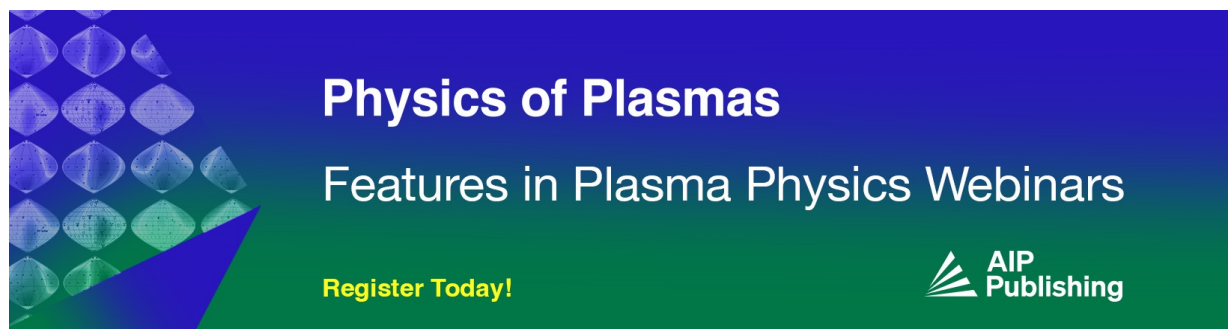
View Online   Export Citation   CrossMark

Physics of Plasmas

Features in Plasma Physics Webinars

Register Today!

AIP Publishing

Experimental demonstration of >20 kJ laser energy coupling in 1-cm hydrocarbon-filled gas pipe targets via inverse Bremsstrahlung absorption with applications to MagLIF

B. B. Pollock,[1,a)] C. Goyon,[1] A. B. Sefkow,[2,3,4,5] M. E. Glinsky,[2] K. J. Peterson,[2] M. R. Weis,[2] E. G. Carroll,[1] J. Fry,[1] K. Piston,[1] A. J. Harvey-Thompson,[2] S. B. Hansen,[2] K. Beckwith,[2] D. J. Ampleford,[2] E. R. Tubman,[1] D. J. Strozzi,[1] J. S. Ross,[1] and J. D. Moody[1]

AFFILIATIONS

[1]Lawrence Livermore National Laboratory, 7000 East Ave., Livermore, California 94550, USA
[2]Sandia National Laboratory, 1515 Eubank SE, Albuquerque, New Mexico 87123, USA
[3]Laboratory for Laser Energetics, 250 E. River Rd., Rochester, New York 14623, USA
[4]Department of Mechanical Engineering, University of Rochester, Rochester, New York 14623, USA
[5]Department of Physics and Astronomy, University of Rochester, Rochester, New York 14623, USA

[a)]Author to whom correspondence should be addressed: pollock6@llnl.gov

ABSTRACT

Laser propagation experiments using four beams of the National Ignition Facility to deliver up to 35 kJ of laser energy at 351 nm laser wavelength to heat magnetized liner inertial fusion-scale (1 cm-long), hydrocarbon-filled gas pipe targets to ∼keV electron temperatures have demonstrated energy coupling >20 kJ with essentially no backscatter in 15% critical electron density gas fills with 0–19 T applied axial magnetic fields. The energy coupling is also investigated for an electron density of 11.5% critical and for applied field strengths up to 24 T at both densities. This spans a range of Hall parameters $0 < \omega_{ce}\tau_{ei} \lesssim 2$, where a Hall parameter of 0.5 is expected to reduce electron thermal conduction across the field lines by a factor of 4–5 for the conditions of these experiments. At sufficiently high applied field strength (and therefore Hall parameter), the measured laser propagation speed through the targets increases in the measurements, consistent with reduced perpendicular electron thermal transport; this reduces the coupled energy to the target once the laser burns through the gas pipe. The results compare well with a 1D analytic propagation model for inverse Bremsstrahlung absorption.

Published under an exclusive license by AIP Publishing. https://doi.org/10.1063/5.0120916

I. INTRODUCTION

Inertial confinement fusion (ICF) in the laboratory is a grand challenge in the high energy density (HED) science community. ICF refers to the process of compressing and heating fusionable fuel (most commonly deuterium or mixtures of deuterium and tritium due to their high fusion cross sections) to pressures at which fusion reactions become sufficiently abundant as to release more energy than was used to assemble the fuel. Currently, there are several approaches being pursued to achieve this goal, including magnetic direct drive (MDD),[1] laser direct drive,[3] and laser indirect drive.[4] The latter two schemes, respectively, use lasers to compress and heat spherical fuel capsules, either by directly illuminating the capsule or by heating a high-Z cylinder (*Hohlraum*) to convert the laser light to x-rays, which then irradiate the capsule. MDD concepts, by contrast, utilize the magnetic drive pressure supplied by a pulsed power generator to compress the fuel. Magnetized Liner Inertial Fusion (MagLIF)[1,5] is one such approach that employs a cylindrical fuel geometry that is compressed radially to the axis with a pulsed power driver.

The challenge of MDD fusion concepts is creating a sufficiently hot, dense plasma at stagnation, given the relatively long (∼100 ns) drive times and natural cylindrical geometry of pulsed power. MagLIF addresses these challenges with a three-stage approach, consisting of (1) pre-magnetization, (2) preheating, and (3) compression. First, an axial magnetic field is applied to the target volume. This thermally

insulates the fuel, reducing radial conduction losses to the beryllium liner surrounding the gaseous fuel. Second, the fuel is heated to a few hundred eV temperatures to increase its adiabat, enabling fusion-relevant fuel pressures to be reached by the subsequent cylindrical compression. This is done with a multi-kJ laser that enters axially into the fuel and deposits energy through inverse Bremsstrahlung absorption. Finally, the Be liner and fuel volume are compressed radially by the J × B force supplied by a pulsed power generator to reach ignition conditions. Since the applied magnetic field is also compressed during this process, charged fusion products generated by the fuel column at stagnation are magnetized, relaxing the density requirements for DT fuel self-heating.

Though MagLIF experiments at the 20 MA Z facility have shown promise, to reach multi-MJ yields pulsed power generators delivering currents in excess of 40 MA to the MagLIF target are required.[2] The MagLIF target designs at this scale require preheat energies of 20–30 kJ deposited into a 5 mg/cc D_2 gas, significantly beyond the 1–2 kJ preheat energy at 527 nm laser wavelength and 0.7–1.4 mg/cc (D_2) fuel density that has been demonstrated on Z.[6,7] This increase in required preheat energy and fuel density represents a significant risk to scaling MagLIF experiments since the energy needs to be coupled to the fuel before the laser overshoots the cm-scale length of the target. In addition, laser plasma instabilities including backscatter, filamentation, and self-focusing have not been tested at these conditions.[8]

No facility exists that can perform all three phases of a high-yield MagLIF experiment at scale; individual components such as fuel preheat can be explored separately at different facilities.[8,11,12] This paper describes room temperature experiments performed at the National Ignition Facility (NIF), which employ a single quad to deliver 30–35 kJ of laser energy at 351 nm wavelength to a MagLIF-like gas tube target scaled to give optimal performance with a >40 MA current drive. The targets are filled with hydrocarbon and Ar dopant gases to enable relevant electron densities to be produced at low gas pressures (1–2 atm) without the need for cryogenic cooling that is necessary for D_2-filled targets (since D_2 has 21 × fewer electrons/molecule than C_5H_{12}, room temperature operation would require 21 × higher pressures for the same electron density, which then requires extremely thick laser entrance windows to hold the pressure). Solenoidal coils coupled to the NIF fast pulsed power system[13] are used to generate up to 24 T applied B-fields to the target length. The experiments demonstrate for the first time that laser energies >20 kJ can be coupled into the gas at the target parameters required for scaled MagLIF designs while producing no measurable laser plasma interaction (LPI) backscatter during the preheating. These results compare well with an analytical model for inverse Bremsstrahlung absorption of the laser energy, providing insight into scaling for future experimental designs. This work extends the energy delivery well beyond previous experiments at Z[6,7] or Omega[8,11,12] while keeping the electron density above and the laser intensity below previous NIF experiments with shorter targets designed to study filamentation onset.[20] The data also demonstrate the impact of magnetic fields, which tend to increase the penetration depth of the laser and reduce the energy coupled. The data suggest that MagLIF on a >40 MA pulsed power facility could be effectively preheated with a NIF quad-like laser.

The remainder of this paper is organized in the following manner: Sec. II describes the experimental setup and the laser energy coupling results, Sec. III compares the unmagnetized results to a 1D analytical propagation model, Sec. IV describes the magnetized results, and Sec. V presents conclusions and future work.

II. EXPERIMENTAL SETUP AND LASER ENERGY COUPLING TO THE TARGET

Figure 1 shows the optimal conditions for fill density and preheat energy as a function of pulsed power driver current for high-yield
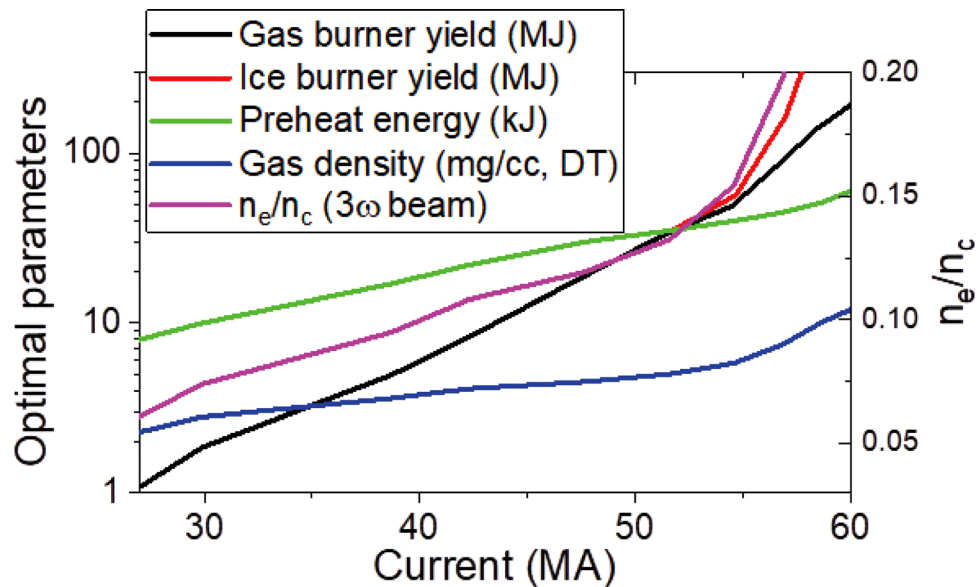

FIG. 1. The optimal values of the electron density (purple, right axis), gas density (blue), and preheat energy (green) with initial 30 T magnetic field are plotted as a function of peak drive current derived from a series of 2D LASNEX simulations, with resulting yields (red and black). Modified with permission from Slutz *et al.*, Phys. Plasmas **23**, 022702 (2016). Copyright 2016 AIP Publishing.

MagLIF designs as determined by 2D Lasnex simulations.[2] The goal of the NIF MagLIF experimental platform is to test preheat in the conditions shown in Fig. 1 for 40–50 MA peak currents. To first order, the key parameter for MagLIF preheat is the energy deposited within the imploding length of the target. Simulations suggest that the target performance is relatively insensitive to small differences in the initial radius and axial uniformity that laser preheat may produce in the fuel because there is sufficient time between preheat and stagnation (~60 ns) for the energy in the fuel to homogenize. For this reason, the results of this study will largely focus on energy coupling metrics with measurements of beam propagation and temperature being used to gain understanding of physical processes.

The target consists of a 1 cm-long, 8.5 mm inner diameter epoxy (Epon 815-C) tube with 100–150 μm thick walls and endcaps with 5 mm diameter central apertures over which 1–1.5 μm thick kapton windows are glued to the entrance and exit ends of the tube; a typical unmagnetized target is shown in Fig. 2(a). Two gas lines fill the target
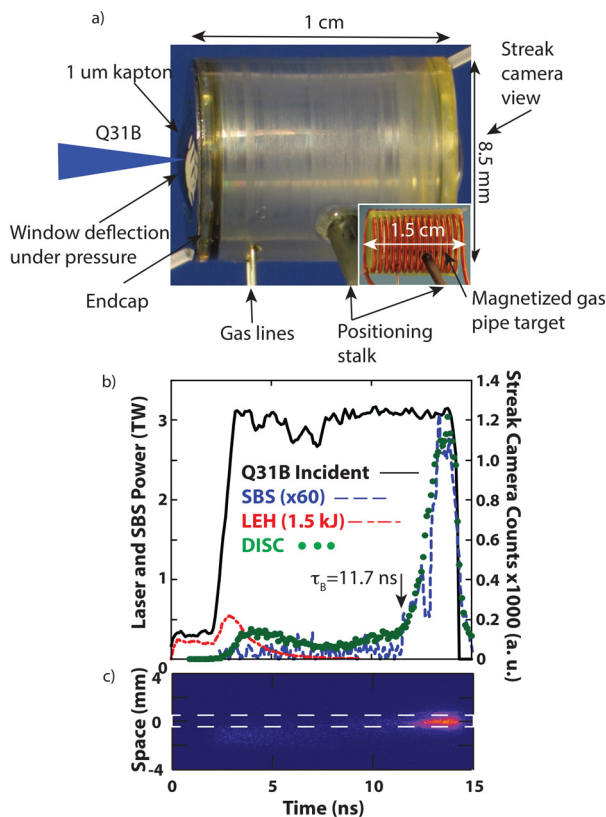

a)

1 cm

1 um kapton

Q31B

Window deflection under pressure

Endcap

Gas lines

Positioning stalk

Streak camera view

8.5 mm

1.5 cm

Magnetized gas pipe target

b)

c)

Q31B Incident —
SBS (x60) – – –
LEH (1.5 kJ) – · – ·
DISC • • •

τ_B=11.7 ns

Space (mm)

Time (ns)

FIG. 2. (a) Photograph of a nominal gas pipe target. Inset: a corresponding image of a target with a solenoid to supply a pre-imposed axial magnetic field. (b) The laser pulse shape for the gas pipe drive (solid black) with the measured Brillouin (SBS) laser backscattered power (dashed blue, multiplied by 60×), estimated power coupled to the laser entrance hole (LEH) window material (dotted red) from simulations (totaling 1.5 kJ), and streaked x-ray emission from the exit window measured with a DISC (DIM-Inserted Streak Camera, dotted green, right axis) for NIF shot N160710. (c) Streaked x-ray emission image from the back window viewed from the chamber polar direction. The white dashed region indicates the location of the lineout shown in (b).

with 1–1.6 atm of a mixture of neopentane, propane, and Ar at room temperature. These gas fills have many hydrodynamic similarities to a pure D_2 fill but can be fielded at low pressure (allowing for thin windows) while at room temperature (accommodating the current NIF capability for magnetic fields). The fully ionized electron density is 11.5%–15% of the critical density $n_c = 9.1 \times 10^{21}$ electrons/cm^3 for the drive laser wavelength of 351 nm.

The NIF lasers enter the target chamber in groups of four beams, arranged in 2 × 2 sets termed quads. The target is positioned at the center of the target chamber and oriented with its axis along that of a single NIF quad (Q31B) whose central spherical coordinates are 150°–236° (polar–azimuthal). The result is that the gas pipe axis is tilted 30° from the target chamber polar axis. The gas pipe is irradiated by all four beams of Q31B, which together are focused at the center of the gas pipe to an elliptical spot size of 1.2 mm× 1.65 mm via the use of standard indirect drive phase plates in each beam line.[14] The individual beams are f/20.7 focusing, but the four together behave as an f/7.9 system to within a few centimeters of best focus, where there is a speckle intensity pattern. The beams also implement polarization smoothing and use 45 GHz of smoothing by spectral dispersion to provide more uniform intensities.[22] The beams nominally have the pulse shape shown in Fig. 2(b) (which corresponds to the delivered Q31B laser power for NIF shot N160710) with a short, low power (0.3 TW) foot to blow down the entrance window, followed by a longer, higher power (3 TW) portion that burns through the gas inside the pipe. For 3 TW peak power, the laser intensity is 1.9 × 10^{14} W/cm^2 with the phase plate spot size (significantly lower than in typical ICF *Hohlraums*).

The primary measurement in these experiments is the laser energy coupling to the target, as preheat energy is a key metric for future MagLIF designs. Each experiment must, therefore, account for the energy delivered to the target, backscattered out of the target, and escaped from the target exit plane. NIF provides precision measurements of the delivered laser power and the backscattered energy [as shown in Fig. 2(b)], where the backscatter is well characterized by full-aperture backscatter station (FABS[23]) and near backscatter imager (NBI[24]) diagnostics. In the absence of a transmitted beam diagnostic (calorimeter, diode, etc.), the time required for the laser to begin irradiating the target exit window can instead be measured using an x-ray streak camera [a NIF DIM-Inserted Streak Camera (DISC[15])] to record emission from that surface. As a conservative estimate, if the time at which burnthrough is first observed (τ_B) is taken to be the end of the experiment, the energy coupling to the target can be estimated by integrating the delivered laser power less any backscatter until this time, $E_{Target} = \int_0^{\tau_B} (P_{Laser} - P_{Backscatter}) dt$. This then directly relates the laser burnthrough time with the laser energy coupling to the entrance window material plus the plasma preheating, where $E_{Target} = E_{window} + E_{preheat}$. The preheat energy is all energy deposited into the fuel, which, in addition to increasing plasma temperature, also accounts for other effects including ionization and subsequent losses such as re-radiated Bremsstrahlung. However, for first order comparisons to MagLIF design work, the coupled preheat energy metric will be used throughout the remainder of the discussion presented here.

The data from N160710, where the streak camera resides in the target chamber upper polar direction (0–0), are shown in Fig. 2(c), with a white-dash boxed region over the central 500 μm of the image. For this experiment, the exit window has been replaced by a thicker,

5 μm kapton foil with 0.3 μm of Ta on the interior side, and the DISC is filtered with 10 μm of Mo to be most sensitive to x-ray emission from 2 to 2.5 keV. The target is filled to 1200 Torr with a 55/43/2 mixture (by partial pressures) of $C_5H_{12}/C_3H_8/Ar$, giving a fully ionized electron density of 15% critical. Figure 2(b) shows a temporal lineout averaged over this region, where the signal rises rapidly at 11.7 ns. Taking this as the burnthrough time, this corresponds to 27.2 kJ of laser energy coupled to the target, assuming no additional heating after the exit window irradiation begins. This level of preheat is consistent with the 40–50 MA range in Fig. 1 for high gain MagLIF experiments.

The temporally resolved stimulated Brillouin scattering (SBS) backscatter signal is shown in Fig. 2(b) below the delivered laser power (multiplied by 60× for clarity), and is essentially noise until the DISC signal rises at 11.7 ns; both signals then fall when the laser turns off between 14.3 and 14.6 ns. This turn on time of the backscattered signal is consistent with the DISC signal for the laser reaching the target exit plane, where the SBS during the laser propagation through the target is below the detection threshold [10's of Joules, as is stimulated Raman scattering (SRS)]. The NBI SBS measurement also shows only noise, reducing the likelihood of scatter at angles larger than the FABS collection cone. Montgomery[16] provides a conservative estimate for the intensity threshold of SBS in a single ion species plasma [Eq. (A11)] that for the densities reported here is $\sim 1.5 \times 10^{14}$ W/cm^2 per millimeter of plasma scale length at 1 keV. Higher electron temperatures or density reductions from hydrodynamic expansion increase this threshold, as does the additional ion Landau damping associated with multiple ion species.[17] For a peak intensity of 1.9×10^{14} W/cm^2, strong SBS is not anticipated. The hypothesis for the appearance of backscatter at the exit plane and not at the beginning of the experiment is attributed to the Ta coating and thicker foil of the exit window compared to the entrance side (1 μm kapton), and to the laser pulse being at peak power (compared to the order of magnitude lower power at the beginning of the pulse when the laser is interacting with the entrance window). Only the experiments with the thicker exit windows (N160128, N160425, and N160710) record SBS above ~ 10 J, and the signal always corresponds within instrument timing uncertainty (few-100 ps) to the rise of the DISC signals; this sets a maximum error bar on the backscatter losses of 250 J for these measurements. The estimate of the energy coupling from the DISC measurement includes laser deposition into the entrance window, which is estimated from simulations to be of order 1–2 kJ. Current experiments are starting to quantify the laser energy coupling into the plasma using the NIF VISAR system, reducing the uncertainty in the coupling measurements.

Figure 3 shows the measured burnthrough time and the laser energy coupled to the target for a series of experiments using this gas fill with increasing applied axial magnetic fields as well as a similar series for 760 Torr gas fills with 99/1 C_5H_{12}/Ar, corresponding to 11.5% critical electron densities. For the unmagnetized 15% critical fills, the energy coupling is well above 20 kJ, even accounting for window losses. These results of higher energy coupling with increased density and reduced coupling with increasing magnetic field are consistent with simple scalings and will be considered quantitatively in future sections by developing a 1D analytic model for the laser propagation.

To understand the overall propagation characteristics of the laser in the target (not just the burnthrough time), plasma self-emission is also recorded on each experiment. An equatorial gated x-ray detector (a NIF GXD[18,19]) collects x-ray emission from the target via pinhole
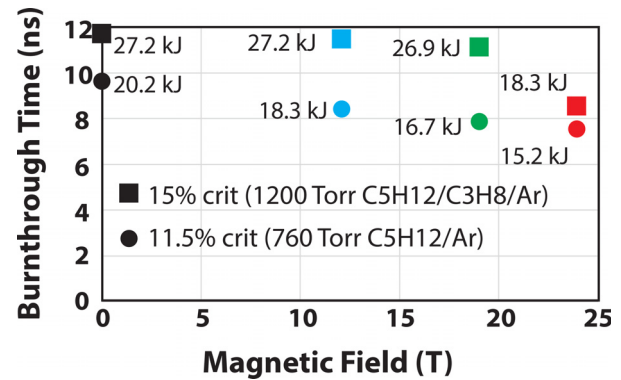

FIG. 3. The burnthrough time with the coupled energy E_{Target} for each of four magnetic field strengths at each of the two fill densities described. The vertical error bar from the DISC resolution corresponds to 200 ps timing uncertainty and is smaller than the size of the points, which corresponds to a ± 750 J uncertainty in the energy coupling. The 11.5% crit, 12 T data point is based on SBS timing rather than end-on burnthrough due to a contaminated signal on the DISC. The 15% crit, 24 T data point also has a larger error bar (1.5 ns or 4.5 kJ) than the rest due to a similar issue, but without an SBS record available to use instead.

imaging onto four independent active areas (strips) on a charge-coupled device camera. Each image has 50 ps temporal resolution, and for 100 μm diameter imaging pinholes with 1× magnification, the spatial resolution is 200 μm. The x-rays emitted from the plasma inside the target are first attenuated by the 100 μm thick epoxy target wall and then subsequently by a 25 μm kapton filter [as in Figs. 4(a)–4(e)]; the combined attenuation of the target wall and the filter convolved with the spectral response of the GXD makes these images most sensitive to x-ray emission between 2 and 8 keV. Emission through additional filter channels on each strip of 175 and 500 μm kapton is also recorded and allows estimates of the temperature. If the plasma emission is assumed to have a spectral profile of the form e^{-E/T_e} that is then convolved with the attenuation and detector response, the integral of photon energies E provides a signal level per pixel at the detector for a given temperature. The ratio of the calculated signal through the 25 and 175 μm channels and the 175 and 500 μm channels is most sensitive between 0.75 and 2 keV. Comparing the ratios of the measured signals with the calculations can then allow temperature estimates along the propagation direction at each strip time. However, since the filters are all kapton without edges in their responses, the error bars toward higher temperatures are substantial. In general, for experiments similar to the configuration in Fig. 2, the temperature is estimated to be 1–1.5 keV, with error bars down to ~ 0.5 keV and extending toward 4–5 keV on the high temperature end. These are consistent with estimates by Glenzer et al.[20] in previous NIF gas pipe experiments and are also the correct order of magnitude, assuming 20 kJ of laser energy is coupled to plasma by the burnthrough time and converted to electron thermal energy in a cm-long column with a cross-section equivalent to the laser spot size.

There are several features of note in the GXD images, where Fig. 4 shows the emission recorded at each time from N160128 (11.5% critical density). This experiment has a nominally identical laser and target configuration to N160710, and similar SBS losses. The images are registered with z = 0 corresponding to the plane of the entrance window without deflection from pressurization. Caps on the ends of
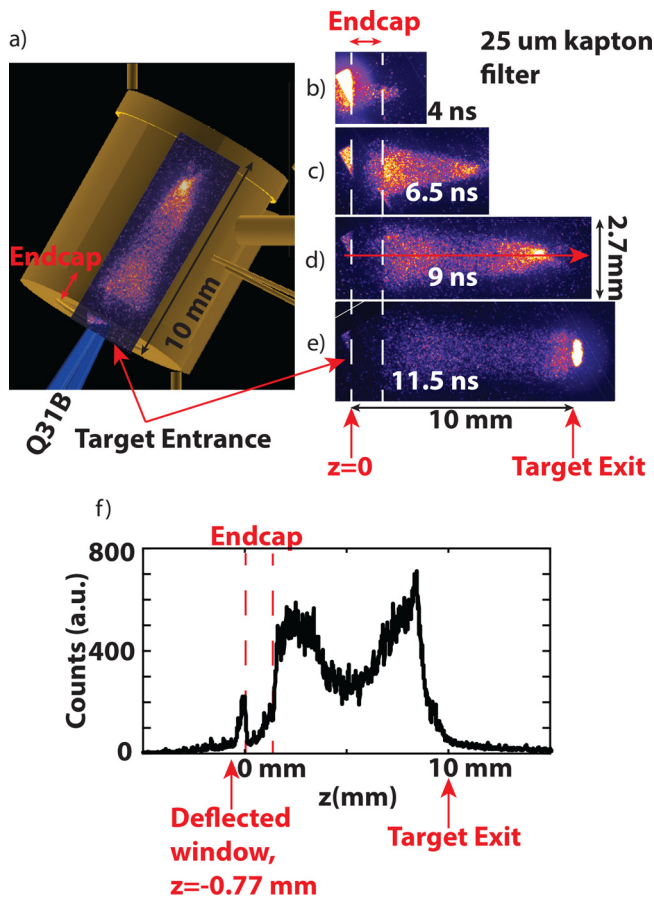
FIG. 4. (a) Computer aided design (CAD) rendering of the target geometry viewed from the GXD line of sight toward 90-315 (polar–azimuthal angle in the target chamber), where Q31B enters from the lower left as indicated. The image from panel (d) is the inset for the scale. (b)–(e) Measured plasma emission profiles at four different times filtered by $25\,\mu m$ of kapton in front of the detector plane. (f) A lineout of the data in panel (d), integrating radially over all emission at each axial location.

the cylindrical tube portion of the target (which hold the windows in place) provide spatial fiducials in the x-ray images. These rexolite endcaps are $200\,\mu m$ thick and extend 1.2 mm from the planes of the windows toward the center of the tube. This additional thickness of plastic significantly attenuates x-rays below 4 keV, creating a lower brightness region just to the interior of both window planes; this is indicated on the entrance side in Figs. 4(b)–4(e) with the white dotted vertical lines. The lower edge of this region is visible at all times recorded, allowing it to be used as an *in situ* reference for the change in the length of the emission between any two times. The bright signal ahead of this region corresponds to emission from CH just outside the target entrance plane; under pressure, the windows deflect outward by a calculated $770\,\mu m$ for the conditions of this experiment (1 atm gas fill, 5 mm diameter aperture, $1\,\mu m$ thick kapton; the calculated deflection under 1200 Torr fill pressure is 1 mm). In the 11.5 ns data [Fig. 4(e)], another bright feature is observed on the right side of the image, corresponding to the exit window of the target being irradiated by the laser. This is consistent with SBS and DISC measurements for this experiment

showing a burnthrough time of 9.6 ns. This system allows spatially and temporally resolved measurements of the location of the front of the heated region throughout the laser propagation, which can be compared to simulations and analytic predictions.

Experiments have also been performed at both of the densities described above with magnetic fields supplied by the new MagNIF pulsed power system.[21] MagNIF utilizes a $4\,\mu F$ capacitor at charge voltages up to 30 kV to supply $\sim$30 kA currents to $\sim\mu H$ inductive loads (or up to 24 T for these gas pipe targets). For the MagLIF experiments, a solenoid of 26 gauge copper wire is wrapped with a pitch of 1 turn/mm along a 14 mm length centered at the midplane of the gas pipe target. The wire diameter is such that the x-ray imaging clear aperture is $\sim$40% of the coil-free target. The axial magnetic field profile is peaked at the center of the gas pipe, decreases by 20% from the midplane to the endcap planes, and is characterized in an offline testing lab. The DISC and GXD systems are compatible with the use of MagNIF, and Fig. 3 shows the coupled energies with each applied B-field strength. At 15% critical, the energy coupling appears unaffected by the magnetic field until it exceeds 20 T. For the 11.5% critical data, the field impact is observed at the lower initial B-field. This will be discussed further in Sec. IV.

III. COMPARISON WITH 1D ANALYTIC PROPAGATION MODEL (B = 0)

To better understand the laser propagation data, the 1D analytical model of inverse Bremsstrahlung absorption proposed by Denavit and Phillion[25] can be considered. In this approach, the laser couples to the plasma according to $\frac{\partial I}{\partial z} = -\kappa I$, where I is the incident laser intensity propagating along the z-axis and the inverse Bremsstrahlung absorption coefficient,

$$\kappa = \frac{1}{c}\frac{n_e}{n_c}\frac{\nu_{ei}}{\left(1 - \frac{n_e}{n_c}\right)^{1/2}} = \kappa^* \frac{n_e^2}{T_e^{3/2}}, \qquad (1)$$

$$\kappa^* \equiv \frac{4\sqrt{2\pi}}{3(4\pi\epsilon_0)^2}\frac{e^4}{cn_c m_e^{1/2} k_B^{3/2}}\frac{Z^* \ln\Lambda}{\left(1 - \frac{n_e}{n_c}\right)^{1/2}}, \qquad (2)$$

where c is the vacuum speed of light, n_e is the electron density, n_c is the critical electron density for the laser wavelength, ν_{ei} is the electron-ion collision frequency, $Z^* = \langle Z^2 \rangle / \langle Z \rangle$ is the ion charge state, e is the elementary charge, $\ln\Lambda$ is the Coulomb logarithm, ϵ_0 is the permittivity of free space, m_e is the electron mass, T_e is the electron temperature, and k_B is the Boltzmann constant. This can be recast as $\kappa = \kappa^* n_e^2 / T_e^{3/2}$ to highlight the dependencies on electron density and temperature and to neglect the weak dependence of κ^* on n_e and T_e. The plasma is assumed to have a constant electron density and to have $n_e/n_c \ll 1$; the model further excludes hydrodynamic motion, ion thermalization, and heat conduction. With these assumptions, the electron energy equation becomes $\frac{3}{2}n_e k_B \frac{\partial T_e}{\partial t} = \kappa I$, which allows for a determination of the location of the laser front with time,

$$z_f(t) = \frac{2}{3}\left(\frac{5}{3}\right)^{3/5}\left(\frac{I_0 t}{n_e}\right)^{3/5}\left(\frac{1}{\kappa^* n_e^2}\right)^{2/5} \propto \frac{(I_0 t)^{3/5}}{\lambda^{4/5} n_e^{7/5}}, \qquad (3)$$

(see Ref. 25 for the complete derivation) with I_0 the incident laser intensity into the target and assuming a square laser pulse profile with

wavelength λ. This model has been successfully applied and modified for work in a variety of experimental configurations,[11,26,27] but never at the length or energy scales presented here.

The key dependency of this model (for constant laser intensity, plasma density, and charge state) is that $z_f \propto t^{3/5}$. Substituting the parameters of the experiments at 11.5% critical density into z_f (n_e = 1.05×10^{21} cm^{-3}, $I_0 = 1.9 \times 10^{14}$ W cm^{-2} is the intensity at peak power, Z = 4.57 for fully ionized neopentane, and ln Λ is assumed constant at 6.7) yields $z_{f,mm} = 3.69 t_{ns}^{3/5}$. Figure 5(a) shows the measurements of z_f extracted from GXD data for several nominally identical experiments using the lower density gas fill. Additionally, it shows
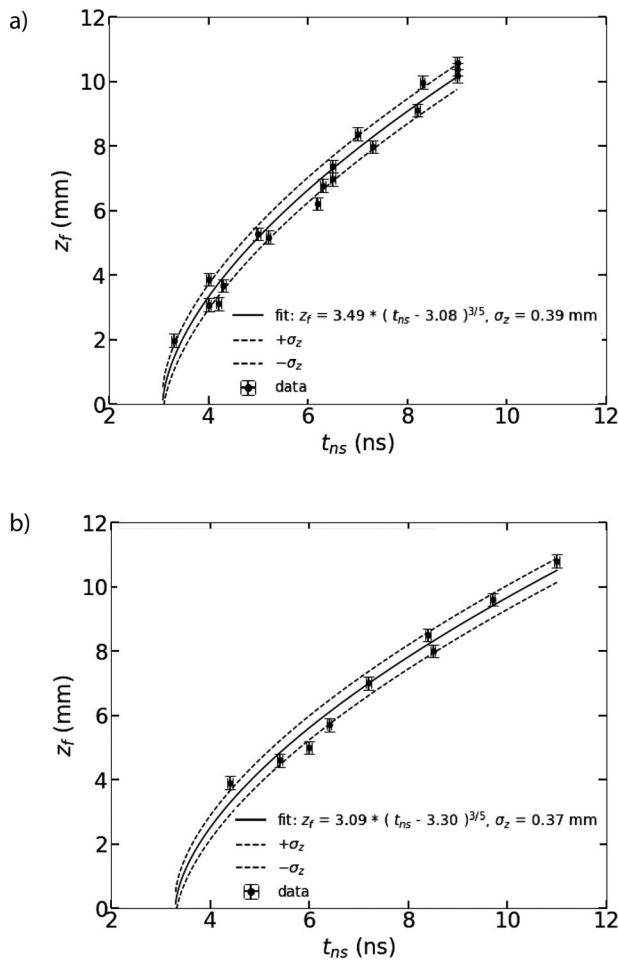
a)

b)

FIG. 5. (a) Measurements (points) of the emission front location from five experiments similar to N160128 (11.5% n_c) are fit with a functional form of the Denavit and Phillion model. The solid curve is the best fit, and the dashed curves represent one standard deviation of fitting error (0.39 mm at a given time). Chi-squared analysis shows $a = 3.49 \pm 0.07$ mm/ns$^{0.6}$ and $\tau = 3.08 \pm 0.8$ ns with a cross correlation of 0.72. Here, z = 0 now corresponds to the calculated deflected entrance window position 770 μm ahead of the undeflected window plane. (b) The same fitting routine is applied to measurements from three experiments similar to N160710 (15% n_c), where the window deflection is 1 mm at the higher fill pressure for this density. For these data, chi-squared analysis results in $a = 3.09 \pm 0.12$ mm/ns$^{0.6}$ and $\tau = 3.3 \pm 0.24$ ns with a cross correlation of 0.86.

a fit to the data of the form $z_f = a(t - \tau)^{3/5}$, where the τ parameter represents the offset from t = 0 in the data for the beginning of the propagation and a represents all of the other dependencies from Eq. (3). This fit indicates $\tau = 3.08$ ns, which is nearly the time the laser reaches peak power (intended to be 3.3 ns), and then propagates at nominally constant intensity until burnthrough. If this is taken to also represent the duration of the laser interacting with the laser entrance window, it is consistent with the LEH power absorption curve in Fig. 2(a) falling off as the laser approaches peak power. These burnthrough times are comparable to mini-MagLIF experiments on Omega,[28,29] where kapton foils of similar thickness to the gas pipe windows are driven with similar intensities and measure ns-scale laser transmission times. The fit also finds $a = 3.49$, in very close agreement with the analytical value of 3.69. The dominant source of uncertainty in a is the laser power fluctuation, which, at the 10% level, corresponds to 6% uncertainty in a. This model can further be compared with the burnthrough measurements from the DISC; accounting for both of the windows deflecting on N160128, the laser must propagate to z_f = 11.1 mm to reach the exit window. Using the expression for the fit to the data, the laser burnthrough time is 10 ns, close to the measured 9.6 ns burnthrough.

Under the formalism of Denavit and Phillion, the expression for the front location in Eq. (3) depends on the product of laser intensity and propagation time, independent of the laser spot size. The coupled energy is

$$E_c = \int_0^{\tau_B} P_0 dt = \int_0^{\tau_B} I_0 A_{spot} dt = I_0 A_{spot} \tau_B, \qquad (4)$$

where the integration begins when the laser reaches peak power P_0, A_{spot} is the area of the laser spot, and τ_B is the burnthrough time relative to the beginning of peak power. Solving Eq. (3) for $z_f(\tau_B) = L$ (total target length), $\tau_B \sim \lambda^{4/3} n_e^{7/3} L^{5/3}/I_0$. Combining this with Eq. (4), $E_c \sim A_{spot} \lambda^{4/3} L^{5/3} n_e^{7/3}$. This means the only way to increase coupled energy via laser parameters is longer wavelength or larger spot size—with no direct dependence on power or intensity. Glenzer et al.[20] arrived at a similar conclusion for a different reason, where in their gas pipes, filamentation was of interest. They demonstrated that beam spreading due to filamentation stopped the laser propagation, which is consistent with the finding that coupling increases with increased laser spot size. Of course, this only applies if the strong assumptions of the Denavit model hold. This implies a matching condition between pulse width and spot size for a given density and target length; for the experiments in Fig. 5(a), a $\sim$50% increase in spot size area is predicted to slow the burnthrough time to roughly correspond to the end of the laser pulse, and couple $\sim$30 kJ to the target. These expressions can be used to guide the design of future experiments, provided the underlying assumptions of the model are reasonable.

Figure 5(b) shows the results of the same GXD analysis and application of the fitting routine, but for the 15% n_c dataset. The temporal offset in the fit is close to that of the lower density data and still corresponds to the nominal time the laser reaches peak power. Since the gas composition is different at the higher density, the effective charge state is reduced slightly to Z = 4.46, and the Coulomb logarithm is also slightly modified to ln $\Lambda = 6.57$. The predicted expression for the front location for the higher fill density $n_e = 1.37 \times 10^{21}$ cm^{-3} is then $z_{f,mm} = 2.59 t_{ns}^{3/5}$, where the leading coefficient between the fit and the model ($a = 3.09$) now disagrees by 16%.

The model neglects hydrodynamic motion and electron thermal conduction, both of which would give rise to emission outside of the initial laser spot (by moving hot material outward or by heating material at larger radius, respectively). The GXD data in Fig. 4 show emission from regions much larger than the 1.2 mm spot size, suggesting that some of these neglected effects are occurring. Pressure-driven plasma expansion reduces the plasma density near the axis and should result in the laser propagation speed increasing due to the lower local density left behind (reducing energy coupling). Radial thermal conduction has the opposing effect, where the laser is now effectively heating more material and, thus, propagates more slowly (increasing energy coupling). Additionally, the measured x-ray emission shows both radial and axial variation, including a dim region near the center of the images; Glenzer et al.[20] observed similar behavior. While the detailed deposition profiles are not expected to matter as much as the total energy coupling (due to the long thermalization time between the laser drive and the pinch in a future MagLIF design), these features cannot be captured by the 1D model presented in this work. A more detailed modeling effort using the radiation magneto-hydrodynamics code Hydra is underway, which will include all of the effects above self-consistently; that work will be presented in a future publication.

IV. FASTER BURNTHROUGH LEADING TO REDUCED ENERGY COUPLING WITH B > 0

Figure 3 shows the burnthrough time and the coupled energies for each electron density and magnetic field condition measured in this campaign. For the 11.5% n_{crit} data, >20 kJ is coupled without an applied magnetic field, though the coupling reduces to ~15 kJ at the maximum 24 T field. At the higher density, ~27 kJ is coupled to the target with B-fields up to 19 T, with the coupling falling off at 24 T to just under 20 kJ. These energy reductions are the direct result of the burnthrough times being reduced when sufficiently high magnetic fields are applied. These energies have had backscatter removed (though only the unmagnetized experiments had the thicker windows and the <250 J SBS) but still include the energy required to blow down the entrance window.

Magnetizing HED plasmas can have a variety of effects on the plasma conditions, especially for reducing hydrodynamic expansion and electron thermal conduction across the magnetic field lines. The former process is generally characterized by the parameter $\beta = n_e k_B T_e/(B^2/(2\mu_0))$, where small β corresponds to a strong impact from the magnetic field. For the measurements described here, assuming initial densities, $T_e \sim 1$ keV, and the maximum B-field of 24 T, the value of $\beta \gg 1$; the magnetic field pressure does not strongly compete with the plasma pressure and should not strongly affect the hydrodynamics. The initial applied magnetic fields are large compared to self-generated fields produced by the Biermann-battery mechanism, where $\partial\mathbf{B}/\partial t = k_B\nabla T_e \times \nabla n_e/en_e$. For ~keV electron temperature and density and temperature gradient scale lengths of 1 mm, these are of order 1 T/ns. The magnetic field is also assumed to be frozen-in, since for the temperatures and densities of these experiments, the plasma resistivity is $\sim 10^{-8}\,\Omega$ m, corresponding to a diffusion scale length of $\sim 10\,\mu$m in 10 ns.

The effect of magnetic field on thermal conduction is a function of the electron Hall parameter, defined as the product of the electron cyclotron frequency $\omega_{ce} = eB/m_e$ and the electron-ion collision time $\tau_{ei} = 1/\nu_{ei}$. Figure 6 shows the ratio of electron thermal conductivity
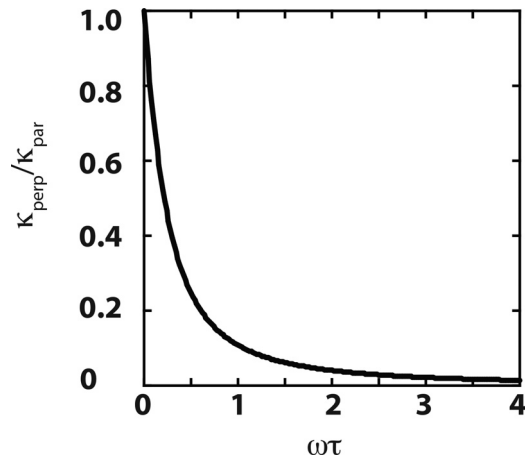

FIG. 6. The perpendicular compared to parallel electron thermal conductivity relative to the direction of the applied magnetic field as a function of Hall parameter for neopentane with Z = 4.57.[30]

perpendicular and parallel to the magnetic field as a function of the Hall parameter for neopentane (and the neopentane/propane mixture since the effective Z is nearly the same for both). For Hall parameter > 0.5, the perpendicular conductivity is reduced by 75% or more compared to the parallel.

Figure 7 shows the calculated Hall parameters for each of the densities as functions of electron temperature for the 12, 19, and 24 T magnetic fields used in the experiments. For all applied field strengths, the Hall parameter reaches 0.5 at electron temperatures of 1 keV (which the Denavit model predicts to be achieved over the first millimeter in the first few hundred picoseconds of peak power) or less, where the perpendicular conductivity should be greatly reduced. As the primary impact of perpendicular electron heat conduction is to slow the laser propagation, reducing the conductivity should lead to faster propagation and reduced energy coupling. This is observed for
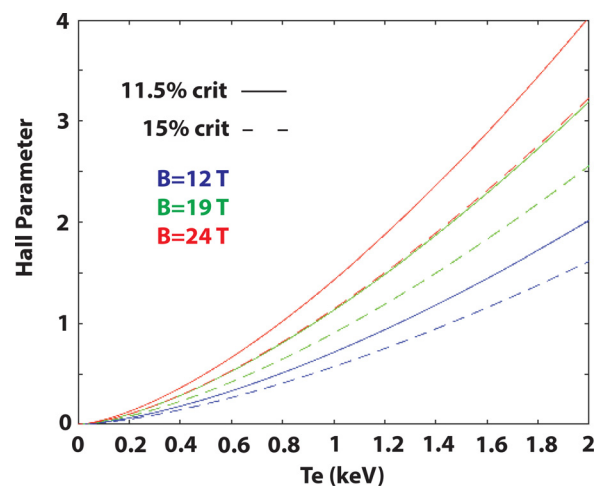

FIG. 7. The Hall parameter for 11.5% (solid) and 15% n_{crit} (dashed) for 12, 19, and 24 T as a function of electron temperature.

all field strengths in the 11.5% n_c data; however, the magnetic field effect on the propagation is not observed until 24 T at 15% n_c. From Fig. 7, the curve for 15% n_c and B = 19 T is bounded by the 12 and 19 T curves for 11.5% n_c, but the 19 T higher density data do not show the expected field effect. These calculations assume constant densities and temperatures and static magnetic fields, not accounting for any B-field advection processes, hydrodynamic expansion, or thermal conduction, which could all modify local parameters.

Additional signatures of modified conductivity are seen in the GXD data of Fig. 8, where the profile of the emitting region becomes more cylindrical when more magnetic field is applied. This behavior has been observed in other magnetized HED experiments,[31–33] where strong fields parallel to the laser propagation resulted in smaller diameter plasmas at higher electron temperatures. Figures 8(a) and 8(b) show GXD measurements for a fixed time (8.3 ns) from B = 0 and B = 12 T in the low-density fill. The white triangles indicate the extent of the emission region, and the half-angle is quoted for each. Figure 8(c) shows the half-angle opening measurements for both densities from 0 to 24 T; in both gas fills, the opening angles decrease with the increasing magnetic field. Just as the effect on burnthrough time and energy coupling is more pronounced in the lower density fill, so too is the effect on the shape of the emitting region. While the change in the shape of the emitting region is present even when there is not a strong modification to the burnthrough time, this is again likely a
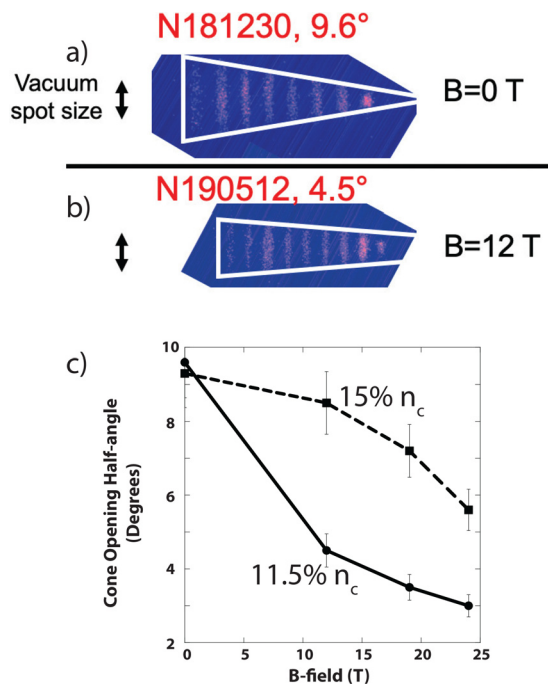
consequence of trying to explain a fairly detailed interaction with an oversimplified model.

Understanding these data requires radiation-hydrodynamic modeling which is ongoing. Two key effects which it includes that the Denavit model does not are hydrodynamic motion and electron thermal conduction. Assuming the heated plasma column's transverse width is much less than its axial length, these two effects are dominantly in the transverse direction, necessitating a 2D model that includes transverse dynamics. It is also expected that the main B-field effect is reducing the transverse electron thermal conductivity. Whether the B-field follows frozen-in flow or is affected by Nernst advection or resistive diffusion is an open question being examined.

V. CONCLUSIONS AND FUTURE WORK

A broad series of experiments examining laser propagation and coupling in MagLIF relevant gas pipe targets has been completed at the NIF. At 15% critical electron density, measurements indicate ∼27 kJ of laser energy can be coupled to the target at magnetic fields up to 20 T. Taking into account losses to blowing down the target entrance window, the coupling to the plasma is still estimated to be >25 kJ. Future experiments will utilize the NIF Visar system to reduce the uncertainty in the energy coupling to the plasma by measuring the evolution of shocks driven in the gas fill. The data compare well with a 1D analytical model for the propagation and provide insight on the impacts of higher order effects not included in the model such as hydrodynamic expansion and electron thermal conduction. The laser propagation is seen to be impacted by having sufficiently high preimposed magnetic fields, whereas the macroscopic behavior of the plasma behind the laser front shows the impact of the field at lower field strengths. A detailed analysis using the hydrodynamic code Hydra is underway, which will better account for many of the effects excluded from the 1D model.

The data demonstrate the ability of a NIF quad-like laser to effectively preheat a high-yield MagLIF target without large-scale backscatter or filamentation. While plasma emission is not observed near the target wall in these experiments, future work will specifically examine whether there is appreciable scatter reaching and heating the target interior wall. In particular, making these measurements in D_2 will provide deep insight into the requirement of additional smoothing techniques (such as 2D smoothing by spectral dispersion) and whether low levels of SBS can be maintained in these gas fills. The energy coupled within the target length at 24 T (15.2 and 18.3 kJ for 11.5% and 15% n_c, respectively) is slightly lower than that required by the scaling. If it is assumed that the coupled energy in the magnetized case scales in proportion to that described by Denavit and Phillion, the coupled energy is expected to scale with the spot size, indicating that a modest increase in the spot size could couple the energies required by the scaling analysis. Further comparisons to simulations are warranted however, as are experiments in D_2 gas fills where models predict filamentation with applied magnetic fields.[34]

While the preheat scaling study described in this paper is motivated and guided by the optimized Lasnex simulations at 40–50 MA,[1] other scaling strategies have recently been proposed to scale MagLIF implosions to higher currents on a future facility. One such strategy is similarity scaling first outlined by Schmit and Ruiz.[35] Following a similarity scaling path[9,10] enables designs achievable on Z to be scaled to higher currents while preserving many of the physics regimes already

FIG. 8. (a) The x-ray emission image at 8.3 ns from N181230 (with B = 0) exhibits a conical emission profile with a cone half-angle opening of 9.6°. (b) The x-ray emission image from N190512 (B = 12 T) shows a more cylindrical profile than panel (a), with a cone half-angle of 4.5°. (c) The cone half-angles for the 11.5% n_c (solid line with circles) and 15% n_c (dotted line with squares) data showing that for both densities, the emission profile becomes more cylindrical with the increasing magnetic field.

present in current-day Z experiments (for example, by preserving the regimes of the energy-loss mechanisms near peak burn). This scaling strategy prescribes a different dependence on current delivery for the fuel density, laser energy, and target height compared to the optimized-scaling approach in Ref. 1. For example, a similarity-scaled MagLIF target at 60 MA requires a preheat energy of 35 kJ into a 4 mg/cc, 18 mm long DT fuel,[9] significantly different from the conditions investigated in this paper. Future studies will aim to investigate laser energy coupling into these relatively long, low-density gas fills to assess the feasibility of preheating similarity-scaled MagLIF load designs.

AUTHOR DECLARATIONS
Conflict of Interest

The authors have no conflicts to disclose.

Author Contributions

Bradley Bolt Pollock: Conceptualization (equal); Data curation (lead); Formal analysis (lead); Investigation (equal); Methodology (equal); Project administration (equal); Supervision (equal); Writing – original draft (lead); Writing – review & editing (equal). **Adam James Harvey-Thompson:** Conceptualization (equal); Data curation (equal); Formal analysis (equal); Investigation (equal); Methodology (equal); Project administration (equal); Supervision (equal); Writing – original draft (equal); Writing – review & editing (equal). **Stephanie B. Hansen:** Conceptualization (equal); Investigation (equal); Methodology (equal); Project administration (supporting); Resources (supporting); Supervision (equal). **Kristian Beckwith:** Conceptualization (equal); Funding acquisition (equal); Investigation (equal); Methodology (equal); Project administration (equal); Resources (equal); Supervision (equal); Writing – review & editing (equal). **David Ampleford:** Conceptualization (equal); Funding acquisition (equal); Investigation (equal); Methodology (equal); Project administration (equal); Resources (equal); Writing – review & editing (equal). **Eleanor R. Tubman:** Conceptualization (equal); Data curation (equal); Formal analysis (equal); Investigation (equal); Methodology (equal); Writing – review & editing (equal). **David J. Strozzi:** Conceptualization (equal); Investigation (equal); Methodology (equal); Validation (equal); Writing – original draft (equal); Writing – review & editing (equal). **James S. Ross:** Supervision (equal); Writing – review & editing (equal). **John Douglas Moody:** Conceptualization (equal); Formal analysis (equal); Funding acquisition (lead); Investigation (equal); Methodology (equal); Project administration (lead); Resources (lead); Supervision (lead); Validation (equal); Writing – original draft (equal); Writing – review & editing (equal). **Clement Goyon:** Conceptualization (equal); Data curation (equal); Formal analysis (equal); Investigation (equal); Methodology (supporting). **Adam Sefkow:** Conceptualization (lead); Formal analysis (supporting); Investigation (equal); Methodology (equal). **Michael E. Glinsky:** Conceptualization (equal); Formal analysis (equal); Investigation (equal); Methodology (equal). **Kyle J. Peterson:** Conceptualization (equal); Methodology (supporting); Project administration (equal). **Matthew Robert Weis:** Conceptualization (equal); Investigation (equal); Methodology (equal); Software (lead); Validation (equal). **Evan Carroll:** Methodology (equal). **Jon Fry:** Funding acquisition (equal); Methodology (supporting); Project administration (supporting); Resources (equal); Supervision (equal). **Kenneth Piston:** Methodology (equal).

DATA AVAILABILITY

The data that support the findings of this study are available from the corresponding author upon reasonable request.

REFERENCES

[1] S. A. Slutz, W. A. Stygar, M. R. Gomez, K. J. Peterson, A. B. Sefkow, D. B. Sinars, R. A. Vesey, E. M. Campbell, and R. Betti, Phys. Plasmas **17**, 056303 (2010).

[2] S. A. Slutz, M. C. Herrmann, R. A. Vesey, A. B. Sefkow, D. B. Sinars, D. C. Rovang, K. J. Peterson, and M. E. Cuneo, Phys. Plasmas **23**, 022702 (2016).

[3] J. H. Nuckolls, L. Wood, A. Thiessen, and G. B. Zimmerman, Nature **239**, 129 (1972).

[4] J. Lindl, Phys. Plasmas **2**, 3933 (1995).

[5] M. R. Gomez, S. A. Slutz, A. B. Sefkow, D. B. Sinars, K. D. Hahn, S. B. Hansen, E. C. Harding, P. F. Knapp, P. F. Schmit, C. A. Jennings *et al.*, Phys. Rev. Lett. **113**, 155003 (2014).

[6] A. J. Harvey-Thompson, M. Geissel, C. A. Jennings, M. R. Weis, M. R. Gomez, J. R. Fein, D. J. Ampleford, G. A. Chandler, M. E. Glinsky, K. D. Hahn *et al.*, Phys. Plasmas **26**, 032707 (2019).

[7] M. R. Gomez, S. A. Slutz, C. A. Jennings, D. J. Ampleford, M. R. Weis, C. E. Myers, D. A. Yager-Elorriaga, K. D. Hahn, S. B. Hansen, E. C. Harding *et al.*, Phys. Rev. Lett. **125**, 155002 (2020).

[8] M. Geissel, A. J. Harvey-Thompson, T. J. Awe, D. E. Bliss, M. E. Glinsky, M. R. Gomez, E. Harding, S. B. Hansen, C. Jennings, M. W. Kimmel *et al.*, Phys. Plasmas **25**, 022706 (2018).

[9] D. E. Ruiz, P. F. Schmit, D. A. Yager-Elorriaga, C. A. Jennings, and K. Beckwith, arXiv:2209.14909 (2022).

[10] D. E. Ruiz, P. F. Schmit, D. A. Yager-Elorriaga, M. R. Gomez, M. R. Weis, C. A. Jennings, A. J. Harvey-Thompson, P. F. Knapp, S. A. Slutz, D. J. Ampleford *et al.*, arXiv:2209.14911 (2022).

[11] A. J. Harvey-Thompson, M. R. Weis, D. E. Ruiz, M. S. Wei, A. B. Sefkow, T. Nagayama, E. M. Campbell, J. A. Fooks, M. E. Glinsky, and K. J. Peterson, Phys. Plasmas **27**, 113301 (2020).

[12] J. R. Davies, D. H. Barnak, R. Betti, E. M. Campbell, P.-Y. Chang, A. B. Sefkow, K. J. Peterson, D. B. Sinars, and M. R. Weis, Phys. Plasmas **24**, 062701 (2017).

[13] C. Provencher *et al.*, "A pulsed power system for magnetized inertial confinement fusion and high-energy density science experiments at the National Ignition Facility" (unpublished).

[14]C. A. Haynam, P. J. Wegner, J. M. Auerbach, M. W. Bowers, S. N. Dixit, G. V. Erbert, G. M. Heestand, M. A. Henesian, M. R. Hermann, K. S. Jancaitis *et al.*, Appl. Opt. **46**, 3276 (2007).

[15]Y. P. Opachich, D. H. Kalantar, A. G. MacPhee, J. P. Holder, J. R. Kimbrough, P. M. Bell, D. K. Bradley, B. Hatch, G. Brienza-Larsen, C. Brown *et al.*, Rev. Sci. Instrum. **83**, 125105 (2012).

[16]D. S. Montgomery, Phys. Plasmas **23**, 055601 (2016).

[17]D. H. Froula, L. Divol, and S. H. Glenzer, Phys. Rev. Lett. **88**, 105003 (2002).

[18]J. A. Oertel, R. Aragonez, T. Archuleta, C. Barnes, L. Casper, V. Fatherley, T. Heinrichs, R. King, D. Landers, F. Lopez *et al.*, Rev. Sci. Instrum. **77**, 10E308 (2006).

[19]J. R. Kimbrough, P. M. Bell, D. K. Bradley, J. P. Holder, D. K. Kalantar, A. G. MacPhee, and S. Telford, Rev. Sci. Instrum. **81**, 10E530 (2010).

[20]S. H. Glenzer, D. H. Froula, L. Divol, M. Dorr, R. L. Berger, S. Dixit, B. A. Hammel, C. Haynam, J. A. Hittinger, J. P. Holder *et al.*, Nat. Phys. **3**, 716 (2007).

[21]J. D. Moody, B. B. Pollock, H. Sio, D. J. Strozzi, D. D.-M. Ho, C. Walsh, G. E. Kemp, S. O. Kucheyev, B. Kozioziemski, E. G. Carroll *et al.*, J. Fusion Energy **41**, 7 (2022).

[22]M. L. Spaeth, K. R. Manes, D. H. Kalantar, P. E. Miller, J. E. Heebner, E. S. Bliss, D. R. Speck, T. G. Parham, P. K. Whitman, P. J. Wegner *et al.*, Fusion Sci. Technol. **69**, 25 (2016).

[23]D. H. Froula, D. Bower, M. Chrisp, S. Grace, J. H. Kamperschroer, T. M. Kelleher, R. K. Kirkwood, B. MacGowan, T. McCarville, N. Sewall *et al.*, Rev. Sci. Instrum. **75**, 4168 (2004).

[24]A. Mackinnon, T. McCarville, K. Piston, C. Niemann, G. Jones, I. Reinbachs, R. Costa, J. Celeste, G. Holtmeier, R. Griffith *et al.*, Rev. Sci. Instrum. **75**, 4183 (2004).

[25]J. Denavit and D. W. Phillion, Phys. Plasmas **1**, 1971 (1994).

[26]J. Faure, V. Malka, and F. Amiranoff, Phys. Rev. E **64**, 026404 (2001).

[27]S. Y. Gus'kov, M. Cipriani, R. DeAngelis, F. Consoli, A. A. Rupasov, P. Andreoli, G. Cristofari, and G. DiGiorgio, Plasma Phys. Controlled Fusion **57**, 125004 (2015).

[28]J. R. Davies, R. E. Bahr, D. H. Barnak, R. Betti, M. J. Bonino, E. M. Campbell, E. C. Hansen, D. R. Harding, J. L. Peebles, A. B. Sefkow *et al.*, Phys. Plasmas **25**, 062704 (2018).

[29]D. H. Barnak, M. J. Bonino, P.-Y. Chang, J. R. Davies, E. C. Hansen, D. R. Harding, J. L. Peebles, and R. Betti, Phys. Plasmas **27**, 112709 (2020).

[30]E. M. Epperlain and M. G. Haines, Phys. Fluids **29**, 1029 (1986).

[31]D. H. Froula, J. S. Ross, B. B. Pollock, P. Davis, A. N. James, L. Divol, M. J. Edwards, A. A. Offenberger, D. Price, R. P. J. Town *et al.*, Phys. Rev. Lett. **98**, 135001 (2007).

[32]S. M. Lewis, M. R. Weis, C. S. Speas, M. Kimmel, R. D. Bengston, B. Breizman, M. Geissel, M. R. Gomez, A. J. Harvey-Thompson, J. Kellogg et al., Phys. Plasmas **28**, 122701 (2021).

[33]K. R. Carpenter, R. C. Mancini, E. C. Harding, A. J. Harvey-Thompson, M. Geissel, M. R. Weis, S. B. Hansen, K. J. Petersen, and G. A. Rochau, Phys. Plasmas **27**, 052704 (2020).

[34]M. R. Weis, A. J. Harvey-Thompson, and D. E. Ruiz, Phys. Plasmas **28**, 012705 (2021).

[35]P. F. Schmit and D. E. Ruiz, Phys. Plasmas **27**, 062707 (2020).